ChemComm

Chemical Communications

rsc.li/chemcomm

ROYAL SOCIETY
OF **CHEMISTRY**
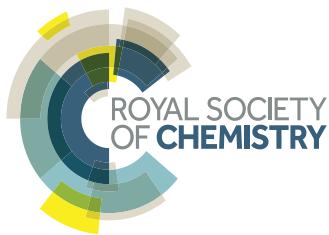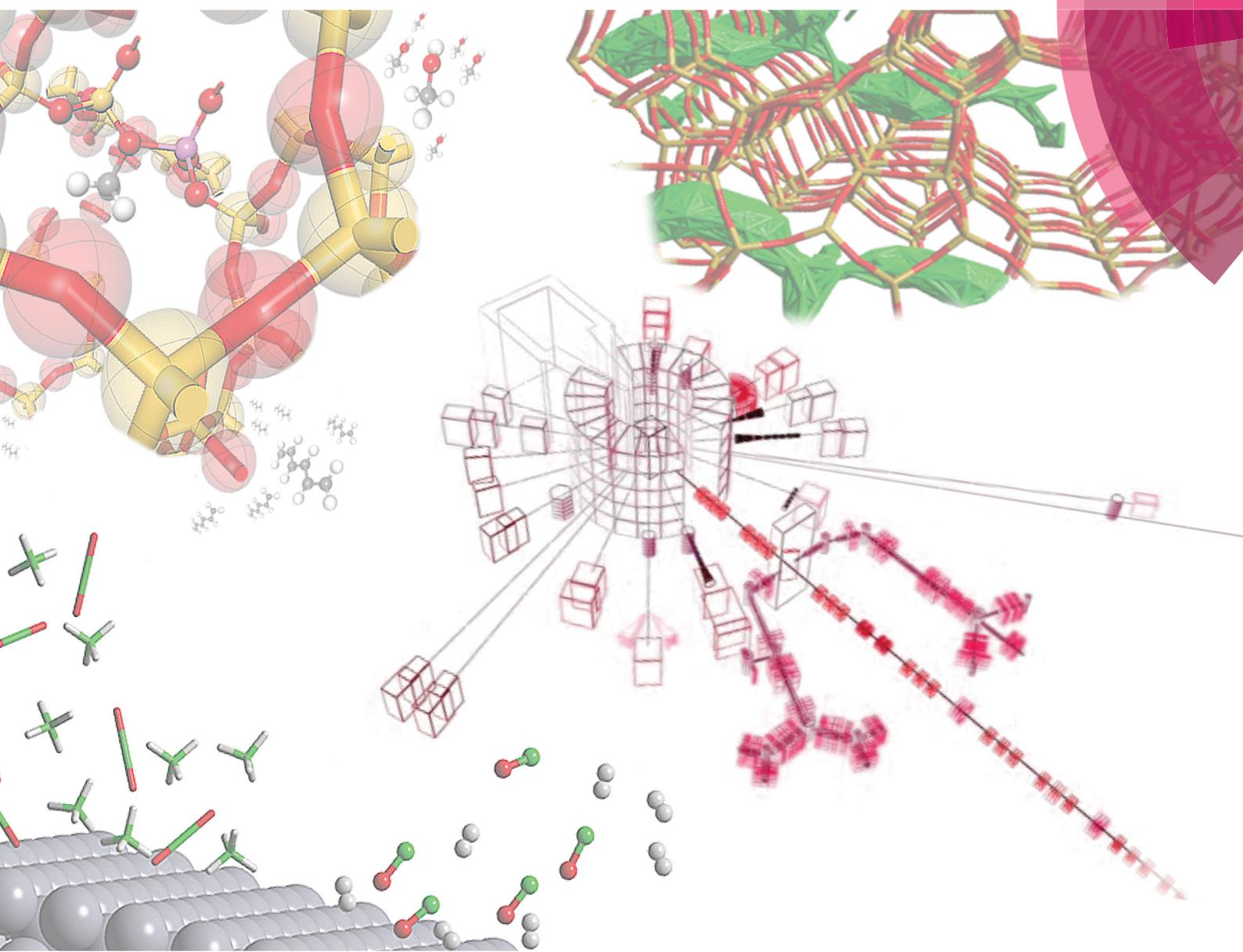
FEATURE ARTICLE
C. Richard A. Catlow *et al.*
Neutron spectroscopy as a tool in catalytic science

ChemComm

Check for updates

Neutron spectroscopy as a tool in catalytic science

Alexander J. O'Malley, [ID] [ab] Stewart F. Parker [ID] [bc] and C. Richard A. Catlow*[abd]

Catalytic science currently has access to a range of advanced experimental methods for the study of molecular behaviour in chemical processes. Neutron spectroscopy, however, is uniquely placed to gain detailed insight into such systems, particularly through techniques such as vibrational spectroscopy with neutrons (INS) which gives access to vibrational modes unavailable to conventional spectroscopy techniques, and quasielastic neutron scattering (QENS) which studies molecular motion on a range of timescales. The present article illustrates the role of these techniques in advancing the field of catalysis. We first provide a brief introduction to the basic principles of the techniques, and then discuss their use in the study of three key catalytic systems: the behaviour of hydrocarbons confined in zeolite catalysts; the methanol-to-hydrocarbons process; and methane reforming. We demonstrate the importance of neutron spectroscopy in understanding established catalytic processes, but also consider its role in the design of future catalytic systems.

1. Introduction

Catalysis is a core area of chemical sciences and as such it is not surprising that key early contributions to the development of the field were made by Michael Faraday. As discussed by John Meurig Thomas in his introductory editorial to this web collection, Faraday was the first to show that platinum surfaces can catalyse the oxidation of hydrogen; and moreover, that this catalytic reaction could be inhibited by pre-adsorption of other species – both vitally important discoveries in catalytic science.

Catalysis, in addition to its huge importance for the economy and for health and the environment, poses exciting fundamental scientific challenges, particularly relating to the understanding of catalysis at the molecular level. The catalytic scientist is, however, fortunate in having a growing range of advanced experimental and computational techniques to elucidate the molecular structures and mechanisms underpinning catalytic processes. This article will highlight the role of neutron scattering in catalytic science, which as we shall show has a unique role to play in elucidating both structure and dynamics in real catalytic systems during their operation; we also show how neutron techniques can be very effectively complemented by computational modelling.

Neutron scattering has a major, and widely recognised role in structural studies of systems with light atoms, especially hydrogen, and as such neutron diffraction has long made a significant contribution to catalysis, especially in determining the positions of adsorbed hydrogen containing molecules in, for example, microporous catalysts,[1,2] more recently even reaction kinetics have been probed with such techniques.[3] The present article will, however focus on the less widely appreciated role of quasi- and inelastic neutron scattering. We will show how quasielastic neutron techniques (QENS) provide key information about hydrocarbon transport processes in microporous catalysts, while inelastic neutron scattering (INS) yields vibrational spectra of adsorbed species which are inaccessible to other techniques and which are vitally important in understanding mechanisms of reaction and deactivation in catalysts. Indeed, while the above techniques have gained significant insight into more established catalysts for bulk chemical production, they are now even being combined to aid the design of more novel microporous catalysts for synthesis of commodity chemicals.[4,5] We will present a brief introduction to the techniques involved before demonstrating their power by examples taken from recent studies. Our focus is on heterogeneous catalysis but the techniques and approaches which we describe are applicable to all branches of the field.

2. Neutron spectroscopy techniques in catalysis

2.1 Vibrational spectroscopy with neutrons

Vibrational spectroscopy is commonly used to study catalysts.[6] The types of investigation range from idealised systems, such as

[a] *Cardiff Catalysis Institute, School of Chemistry, Cardiff University, CF10 3AT, UK.*
   E-mail: CatlowR@cardiff.ac.uk

[b] *The UK Catalysis Hub, Research Complex at Harwell,*
   Rutherford Appleton Laboratory, Oxfordshire, OX11 0FA, UK

[c] *ISIS Facility, STFC Rutherford Appleton Laboratory, Chilton, Didcot, Oxfordshire,*
   OX11 0QX, UK

[d] *Department of Chemistry, Materials Chemistry, University College London,*
   Third Floor, Kathleen Lonsdale Building, Gower Street, London, WC1E 6BT, UK

adsorbates on metal single crystals in ultra-high vacuum, through to working catalysts at industrial conditions of temperature and pressure. Vibrational spectroscopy with neutrons[7] (inelastic neutron scattering, INS) is a form of vibrational spectroscopy that is complementary to conventional methods, *e.g.* infrared and Raman spectroscopies, that has particular advantages for the study of catalysts. In the course of this article, we will highlight some of these. Of course, any technique also has limitations, which will also be discussed.

The differences between INS and infrared/Raman spectroscopies are clearly seen by considering the expression for the intensity of an INS mode:

$$S(Q, n\omega_i) \propto \frac{(QU_i)^{2n}}{n!} \exp\left(-(QU_{\text{Tot}})^2\right)\sigma_{\omega_i} \qquad (1)$$

$$[1] \qquad\qquad [2] \qquad\qquad [3] \qquad [4]$$

where ω_i is the ith mode at transition energy ω, $n = 1$ for a fundamental, 2 for a first overtone or binary combination, 3 for a second overtone or ternary combination *etc...*, Q is the momentum transfer (also referred to as the scattering vector), U_i is the root mean square displacement of the atoms in the mode ω and σ is the inelastic scattering cross section of the atom. U_{Tot} is the total root mean square displacement of all the atoms in all the modes, (both internal and external).

Eqn (1) can be considered to be comprised of four parts. The first part, [1], is the measured intensity, $S(Q,\omega)$ (also referred to as the dynamic structure factor). Note that this depends on two variables: the transition energy and the momentum transfer, Q. The latter arises because a neutron has mass (1.009 amu) and any scattering event will involve a change in momentum (since the neutron will change direction) and may also involve a change in energy, ΔE. If $\Delta E = 0$, then the scattering is purely elastic and gives information about atomic positions, neutron diffraction being an obvious example. However, small angle neutron scattering (SANS),[8] total scattering[9] and neutron reflectivity[10,11] exploit the same property. If $\Delta E \neq 0$, the scattering is inelastic which is the focus of this article. The intensity dependence on Q is the major difference between INS and infrared and Raman spectroscopies, where the modes are observed at (almost) $Q = 0$.

Term [2] shows that the intensity depends on the momentum transfer and the amplitude of vibration of the atoms in the normal mode. Note that it varies as $2n$, this is because overtones and combinations are allowed transitions within the harmonic approximation, another difference to infrared and Raman spectroscopies.

Term [3] is a Debye–Waller factor and its magnitude is, in part, determined by the thermal motion of the system, which can be reduced by cooling the sample and so spectra are typically recorded below 30 K. For *in situ* or *operando* studies of catalysts, this factor is probably the biggest limitation of the technique; thus historically, virtually all INS catalyst studies have adopted a "react and quench" approach.[12] Recent work[13] has shown that in favourable circumstances this approach is not always essential and implementation of *operando* studies is an area of active interest.

The last term is the incoherent scattering cross section of the elements in mode ω, which is both element and isotope dependent and for normal hydrogen, ^{1}H, it is 80.2 barns (1 barn = 1×10^{-28} m^{-2}) whereas for deuterium, ^{2}H, and for virtually all other elements it is <5 barns. INS spectroscopy has no selection rules so in principle all modes are observable. However, the combination of the large cross section of ^{1}H, and that ^{1}H has the largest amplitude of vibration (since it is the lightest isotope), means that there is a strong "propensity" rule that the observed modes are those that involve motion of hydrogen.

Eqn (1) has consequences that are relevant for studies of catalysts. Since neutrons are scattered from atomic nuclei and the nucleus is only $\sim1/1000$ of the diameter of the atom, neutrons only interact weakly with matter and are consequently highly penetrating. Cell design is as a consequence relatively straightforward, in that materials such as steel, aluminium and quartz are all transparent to neutrons. In addition, the spectral cut-off commonly found for infrared spectra of supported metal catalysts (due to absorption by the support's lattice modes) is inapplicable and the entire spectral range 0–4000 cm^{-1} is available. The nuclear scattering also results in INS spectroscopy being relatively insensitive; sample sizes range from ~10 g for a high surface area zeolite or supported metal catalyst, to ~30 g for a metal powder (*e.g.* RANEY®Ni), with a surface area of ~10 m^{-2} g^{-1}. For new materials this limitation can be a drawback, but for industrial catalysts it is not a problem and the use of large samples means that concerns about reproducible sampling are greatly ameliorated, which is regarded by industry as a positive factor for neutron scattering studies. Finally, neutrons are "democratic", so they "see" everything and the spectra are the sum of both the bulk and the surface. Thus INS spectra of catalysts are usually difference spectra and typically, the spectrum of the clean catalyst is used as the background.[14]

2.2 Quasielastic neutron scattering: molecular mobility in catalysis

We now turn to the principles behind determining the mobility characteristics of hydrogenous molecules in catalysis. Our account has been adapted from ref. 15–17. These references also give details of how to characterise localised motions of molecules such as rotation, which are outside the scope of the present article.

The much larger incoherent scattering cross section of ^{1}H hydrogen leads to much larger scattering of the hydrocarbon compared to the inorganic material of a catalyst. The scattering function obtained ($S(\boldsymbol{Q}, \omega)$) is the four dimensional Fourier transform of the self-part of the van Hove correlation function $G_s(r,t)$ – in essence, a probability density in three-dimensional space, that a particle will be displaced by a vector r within time t at equilibrium. In the scattering function, $\boldsymbol{Q}$ and ω are the Fourier transformed variables of r and t. Small $\boldsymbol{Q}$ involves average values over long distances, and slow motions taking place over long times in $G_s(r,t)$, will correspond to small ω. When the characteristic time of the motion is shorter than the inverse of the instrumental resolution, a broadening of the scattering function will be observed. The broadening of the scattering

function must be convoluted with the instrumental resolution function in order to be quantified.

2.2.1 Self-diffusion – isotropic and Jump models. In the case of unhindered, isotropic diffusion as defined by Fick's second law:

$$\frac{\partial p(\boldsymbol{r}, t)}{\partial t} = D_s \nabla^2 p(\boldsymbol{r}, t) \tag{2}$$

where $p(\boldsymbol{r},t)$ is the probability of finding an atom at position $\boldsymbol{r}$ at time t, the aforementioned self-part of the van Hove correlation function $G_s(r,t)$ is the solution. In the case of isotropic diffusion, the scattering function obtained is given by the following Lorentzian function:

$$S(\boldsymbol{Q}, \omega) = \frac{1}{\pi} \frac{D_s \boldsymbol{Q}^2}{\omega^2 + (D_s \boldsymbol{Q}^2)} \tag{3}$$

where D_s is the self-diffusion coefficient. At sufficiently low Q values (larger distances) the half-width at half-maximum (HWHM) of this Lorentzian function has a $D_s Q^2$ dependence; thus a plot of the HWHM as a function of Q^2 will be linear, although this analysis is only valid for larger distances (smaller Q values).

When considering sorbate mobility in microporous catalysts, jump diffusion models are often used. These consider a molecule which is stationary at a site (such as a channel intersection) for a defined period, which then jumps a given distance to another site. At larger momentum transfers, we observe deviations from the linearity of the DQ^2 dependence as the system is not continuous at the shorter length scales probed at these larger Q values.

A model commonly used to describe such behaviour was formulated by Chudley and Elliot[18] which proposes that for an average time interval τ, an atom remains on a given site vibrating about a centre of equilibrium. After this time, the atom moves rapidly to another site in a negligible jump time compared to the time spent at the residence site. The Chudley and Elliott model assumes a constant jump length d, with the Lorentzian HWHM dependence on Q being:

$$\Delta \omega(Q) = \frac{1}{\tau} \left(1 - \frac{\sin(Qd)}{(Qd)} \right) \tag{4}$$

One may then obtain the Fickian diffusion coefficient as at low Q, expanding the sinc function up to the third order in terms of Qd gives us:

$$\Delta \omega(Q) = \frac{(Q^2 d^2)}{(6\tau)} \tag{5}$$

And we can again obtain a DQ^2 dependence with a diffusion coefficient of:

$$D_s = \frac{d^2}{6\tau} \tag{6}$$

Other models, including the Singwi-Sjölander[19] and Jobic[20] models, deal with jump distances which are not constant, but consider a jump length distribution around a mean square jump length.

2.2.2 Neutron spin-echo techniques. Neutron spin echo (NSE) studies can probe timescales two orders of magnitude

longer than conventional TOF/BS instruments.[15,21] However the scarcity of instruments available means that very few studies in catalytic systems are available in the literature.[22–24] The velocities of polarized neutrons are compared before and after the scattering event, using the Larmor precession of the neutron spin. The spin vector acts as an internal timer linked to each neutron, connecting it to the velocity measurement, which allows the velocities before and after scattering of the neutron to be compared, and a direct measurement of the velocity difference can be performed. Experimentally one measures the beam polarisation, the average $\cos \varphi$

$$\langle \cos \varphi \rangle = \int S(Q, \omega) \cos(\omega t) \mathrm{d}\omega = I(Q, t) \tag{7}$$

One can see that NSE measures the intermediate scattering function $I(Q,t)$ (an inverse Fourier transform of $S(Q,\omega)$) so data are actually recorded as a function of time rather than a function of ω as with conventional QENS experiments. In the case of quasielastic scattering, one measures the decay of $I(Q,t)$ as a function of time. When the self-part of the van Hove correlation function can be described by a Gaussian, the spatial Fourier transform yields an exponential function.

$$I(Q,t) = \exp(-DQ^2 t), \tag{8}$$

The diffusion coefficient may then be obtained relatively simply if the diffusion is in the Fickian regime. A time Fourier transform of $I(Q,t)$ results in $S(Q,\omega)$; thus broadenings may be obtained and diffusion coefficients and jump parameters may also be derived as in Section 2.2.1.

An important characteristic of both QENS and NSE experiments is that they sample the same time and length scales as molecular dynamics (MD) simulations. This combination of techniques has proved to give unique insight into molecular behaviour in catalytic systems[15,25–29] and will feature prominently in this article.

3. Hydrocarbon behaviour in MFI zeolite catalysts

The study of hydrocarbon dynamics in zeolite catalysts is of great importance due to its relevance to processes such as cracking of hydrocarbons in the petrochemical industry.[30–33] A significant amount of recent work, both theoretical and experimental, has been carried out studying the diffusion of hydrocarbons in the MFI zeolite structure,[34–45] which is the framework type of the industrially important ZSM-5 and its siliceous analogue, silicalite-1. With these applications in mind, we will discuss studies where QENS (particularly in combination with MD simulations) has gained important insights into straight chain and branched hydrocarbon dynamics in MFI zeolites.

3.1 *n*-Alkane diffusion in silicalite-1 and Na-ZSM-5

The diffusion of longer *n*-alkanes in the MFI framework has been of recent interest and has been studied using QENS in both Na-ZSM-5[46] and silicalite-1.[47] The effect on *n*-octane diffusion
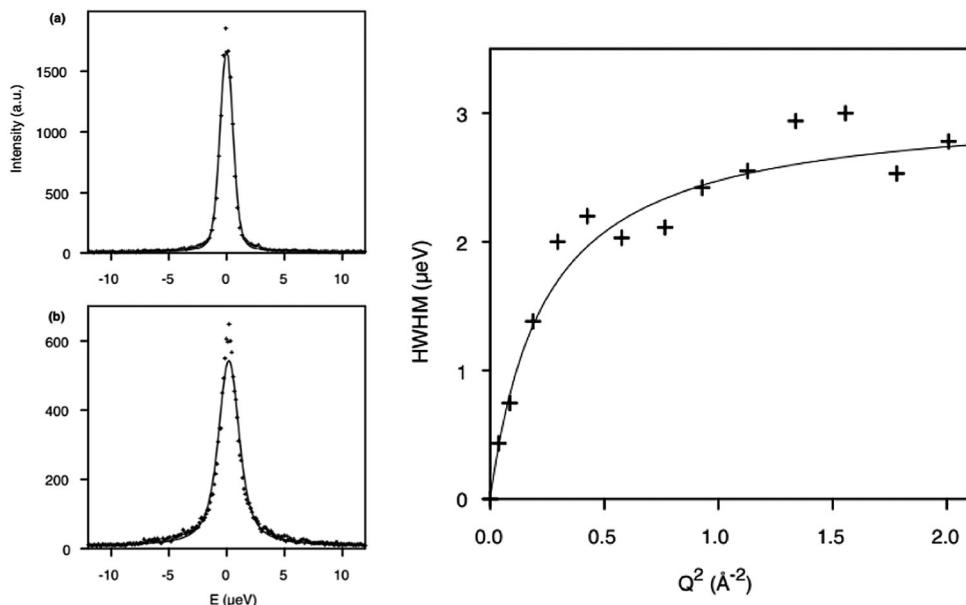
Fig. 1 (left) QENS spectra obtained and fitted for *n*-octane (top) Na-ZSM-5, 0.9 mol/uc and (bottom) silicalite-1 (1.56 mol/ucl) at 300 K. (right) Broadenings derived for QENS spectra and fitted to the Singwi and Sjölander jump diffusion model for *n*-octane in silicalite-1 at 300 K. Reproduced from ref. 48 with permission from Elsevier.

of the presence of extra-framework cations was studied by Leroy and Jobic[48] who measured the diffusion coefficient in both silicalite-1 and Na-ZSM-5. QENS spectra obtained at $Q = 0.29$ Å^{-1} at 300 K in the two materials are shown in Fig. 1 (left), where the broader spectrum in silicalite-1 illustrates the increased mobility over this length scale in silicalite-1. The Singwi and Sjölander jump diffusion model[19] was then used to fit the broadenings as a function of Q as shown in Fig. 1 (right), giving the D_s at 300 K in silicalite-1 of 2.0×10^{-10} m^2 s^{-1}, four times higher than that in Na-ZSM-5, illustrating the extent to which the presence of Na$^+$ counterions decrease the mobility of *n*-octane.

The diffusion of longer *n*-alkanes (C$_8$–C$_{20}$) was also studied in these zeolites.[47] The diffusion coefficients obtained as a function of chain length are plotted against those obtained using other methods including PFG-NMR, MD and hierarchical simulations (which employed coarser grain models) in Fig. 2.[35,47,49,50] The measured values of D_s for the QENS experiments were found to be in very close agreement with hierarchical simulations.

For example, the difference in D_s between simulation and experiment for decane is less than a factor of two, particularly close considering the experimental errors of the QENS values (30% from C$_8$ to C$_{12}$ and 50% for C$_{14}$ and C$_{16}$) and the error associated with the coarse-graining procedures of the simulations. Activation energies obtained as a function of chain length, however, did not quite replicate such a close agreement. Closer agreement with the QENS experiments was found in more recent atomistic molecular dynamics simulations for these systems.[51] Loadings matching experiment were used (therefore accounting for sorbate/sorbate interactions), employing a flexible zeolite framework and explicit atom model of the hydrocarbon, a view of the system is displayed in Fig. 3.
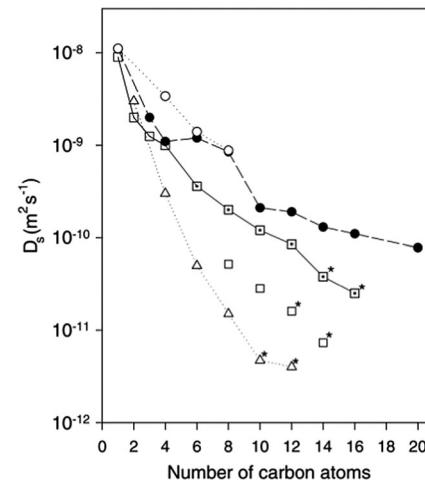
Fig. 2 Self-diffusivities obtained at 300 K from MD simulations (○),[35] hierarchical simulations (●),[50] QENS in Na-ZSM-5 (□),[46] QENS in silicalite-1 (⊡)[47] and PFG-NMR (△).[49] * = extrapolation to 300 K. Figure reproduced from ref. 47 with permission from the American Chemical Society.
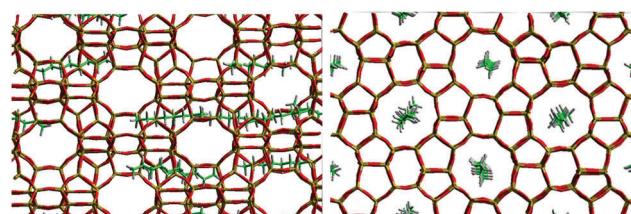
Fig. 3 A view of the system for octane in silicalite-1 pre-production run at 300 K viewed down the (left) 010 direction and (right) 100 direction. Reproduced from ref. 51 with permission from the PCCP Owner Societies.
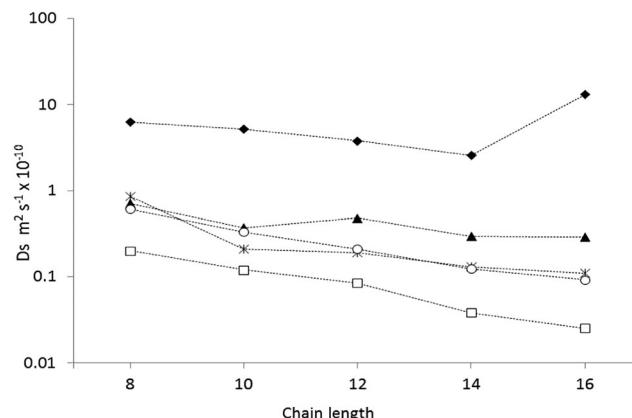
Fig. 4 A plot of the calculated diffusion coefficients from the MD simulations using experimental loadings (O),[57] MD simulations at infinite dilution[53] (▲), MD simulations using more primitive models[52] (◆), Hierarchical simulations[50] (*) and QENS studies[47] (□). Reproduced from ref. 51 with permission from the PCCP Owner Societies.

The diffusion coefficients for all chain lengths at 300 K using QENS, along with simulations of different complexity, are compared in Fig. 4. Our most complex simulations (using a fully atomistic hydrocarbon model, a flexible zeolite framework and experimental loadings) gave the closest agreement, with all the calculated diffusion coefficients, within a factor of five of the QENS measurements, consistently closer to the experimental regime than the simpler models.[50,52,53] As is common when comparing QENS experiments with simulations, the diffusion coefficients obtained by MD are higher than those obtained experimentally, despite the sophisticated model and use of experimental loadings. This discrepancy can probably be attributed to the use of a perfect silicalite-1 crystal in the simulations, allowing for faster, less hindered diffusion on the nanometre scale. The sample used in the QENS experiments would have point defects such as silanol nests and grain boundaries on the nanometre scale as well as surface effects from each crystallite, which are not accounted for under the periodic boundary conditions employed by the simulation.

Activation energies obtained by QENS, together with those for our most complex MD simulations and hierarchical simulations are plotted in Fig. 5. We can see that the trend (a roughly monotonic increase with chain length) of the calculated activation energies, follows that observed by QENS. A significant source for discrepancy between experiment and simulation for the longest alkanes was uncovered by neutron spin-echo experiments.[54] For longer alkanes, redistribution of the molecules throughout the crystal was observed at higher temperatures, allowing the molecules to cross internal barriers and access other parts of the crystal. As the simulations were carried out using periodic boundary conditions, this redistribution behaviour cannot be modelled as the supercells employed cannot be large enough to sample this behaviour. The activation energies in the MD simulations were consistently lower than those obtained by QENS experiments probably due to the factors discussed above relating to defects in the experimental sample. The trend and agreement in activation energies between the
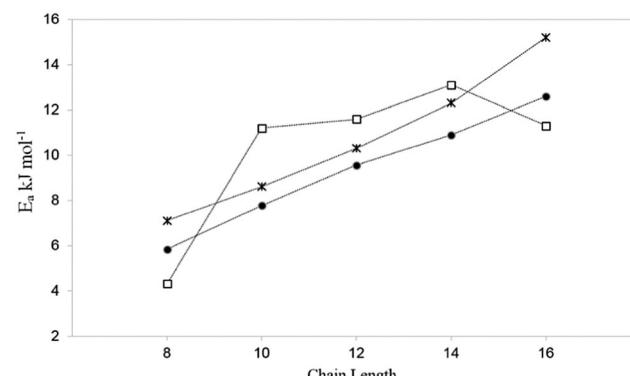
Fig. 5 A plot of the activation energy of diffusion with chain length, for the MD studies at experimental loadings (●),[51] QENS studies[47] (*) and hierarchical simulations (□).[50] Reproduced from ref. 51 with permission from the PCCP Owner Societies.

most sophisticated MD results and the QENS experiments is a marked improvement compared to that of the hierarchical simulations, suggesting that although the coarse-grained method is accurate at 300 K, this accuracy is not maintained at higher temperatures.

3.2 Branched alkane diffusion in silicalite-1 and Na-ZSM-5

Though the majority of work studying molecular diffusion in the MFI framework focuses on n-alkanes, branched alkanes are just as prevalent in fluid catalytic cracking and molecular sieving systems under industrial conditions.[31] Microscopic techniques such as quasielastic neutron scattering have rarely been used to study these systems, mainly due to the low resolution of instrumentation which led previously to significant errors in measured diffusion coefficients for the slower moving branched sorbates. A study of isobutane in ZSM-5 gave diffusivities that were an order of magnitude lower using QENS than supported membrane studies, consistent with previously observed differences between macroscopic and microscopic techniques.[55] The HWHM broadenings of the elastic peak measured for isobutane in ZSM-5 are shown in Fig. 6 (left) along with a QENS spectrum at $Q = 0.87$ Å^{-1} (right). We note that the broadenings are very small with respect to the resolution function (15%) indicating very low mobility (far lower than for longer n-alkanes). At the higher Q values (0.4–0.8 Å^{-1}) the broadenings could be fitted with the Singwi and Sjölander[19] jump diffusion model (the broadenings at low Q were too small to be determined), with a mean jump distance of 4.5 Å and residence time of 6 ns. The self-diffusion coefficient of isobutane in ZSM-5 was found to be about three orders of magnitude lower than that of n-butane in the same zeolite.[56] However, the inability to measure at low Q lead to errors in D_s of a factor of 4, much larger than the usual error, $\sim 50\%$.[56–58]

Recent work has used the neutron spin-echo (NSE) method and fully atomistic MD simulations to measure isobutane diffusion in silicalite-1, in the temperature range of 450–550 K.[59] The simulations were carried out using a contemporary flexible zeolite potential and explicit atom hydrocarbon model as in Section 3.1. Experimentally, the NSE method is especially appropriate because of its ability to measure diffusion coefficients of
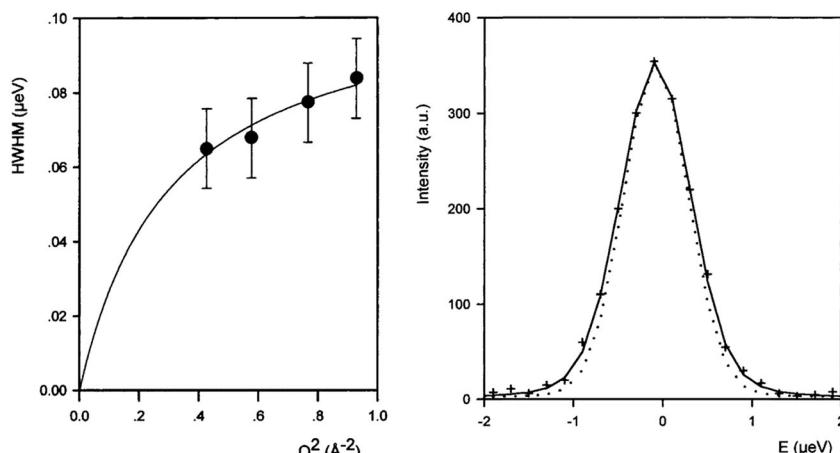
Fig. 6 (left) Broadenings obtained for isobutane in ZSM-5 at 570 K, and QENS spectra obtained at 570 K (Q = 0.87 Å). The dotted line is the resolution function. Reproduced from ref. 55 with permission of the American Chemical Society.

very slow moving sorbates in smaller pore zeolites with very high precision, owing to the high resolution of the instruments. Normalized intermediate scattering functions ($I(Q,t)$) obtained experimentally for isobutane in silicalite-1 at 491 K at Q = 0.2 and 0.3 Å^{-1} are shown in Fig. 7. On comparing 3D and 1D diffusion models, the 3D diffusion model provides a better fit to the experimental points than 1D diffusion, which implies that isobutane molecules are able to explore both straight and sinusoidal channels. The observation contrasts with previous QENS and NSE measurements of n-alkanes longer or equal to C$_8$, which diffuse mainly along the straight channels.[46,54]

Temporal decays extracted from the intermediate scattering functions can be expressed as energy broadenings as shown in Fig. 8, when plotted as a function of Q^2. The trend is characteristic of the Chudley–Eliott jump model[18] with a fixed jump length of 10 Å, previously used in the case of benzene in ZSM-5, which concluded a residence period at the intersection between straight and sinusoidal channels, and jump diffusion between them.[60] The diffusivities were then extracted from the low-Q range.[15]

The experimental diffusion coefficients are plotted in Fig. 9. When compared to the study discussed above of isobutane in ZSM-5,[55] the diffusion coefficients were about one order of magnitude higher in silicalite-1. Counterintuitively, the activation energy measured in ZSM-5 was lower than that in silicalite-1 (17 kJ mol^{-1} in ZSM-5 compared to 22.6 kJ mol^{-1} in silicalite-1). However, since the broadenings were small compared with the instrumental resolution for the ZSM-5 measurements, the errors were much larger than in this study.

On comparison with MD simulations, the calculated diffusion coefficients are all within a factor of 7.5 of experimental results. Diffusion coefficients calculated by MD were in the


Fig. 7 Comparison between experimental and calculated normalized intermediate scattering functions obtained for isobutane in silicalite-1 at 491 K, for Q = 0.2 (▽) and 0.3 Å^{-1} (◇). The solid lines are calculated with: (a) a 3D diffusion model, and (b) a 1D diffusion model. Reproduced from ref. 59 with permission from the American Chemical Society.
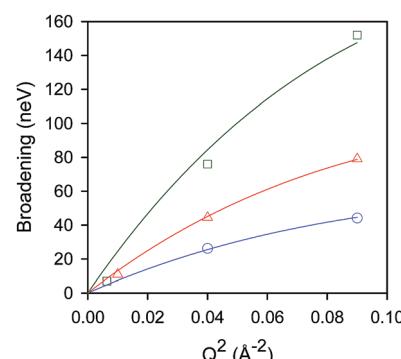
Fig. 8 Broadenings obtained for isobutane in silicalite-1 at: 444 K (○), 491 K (△), and 550 K (□). The solid lines correspond to a Chudley–Elliot jump diffusion model. Reproduced from ref. 59 with permission from the American Chemical Society.
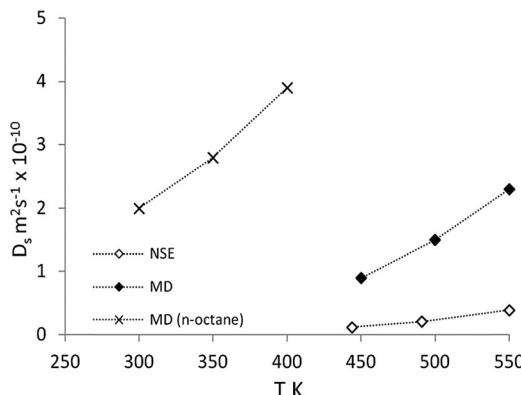
Fig. 9 Comparison of diffusion coefficients of isobutane from NSE (◊) and MD (♦) compared with previous simulations of *n*-octane diffusion in ref. 51 (×). Reproduced from ref. 59 with permission from the American Chemical Society.

upper limit of experimental results, which as in previous section, can be attributed to the use of a perfect periodic silicalite-1 crystal structure in these simulations. The activation energy of diffusion was calculated as 19.2 kJ mol^{-1} : 3.4 kJ mol^{-1} ($\sim$15%) lower than that observed by the NSE experiments.

The mean square displacement (MSD) plot in the possible directions obtained from the MD simulations was examined to observe preference for a specific channel system, which can also be illustrated by the use of a trajectory plot to show specific locations of molecules. The directional MSD plot of a single isobutane molecule at 450 K is shown in Fig. 10, which indicates that the molecule is diffusing in both channel systems, but shows preference for the $\langle 100 \rangle$ direction (the sinusoidal channels), in contrast with *n*-alkanes where the 010 channel is preferred. The ability to explore both the straight and sinusoidal channels would agree with the 3D diffusion observed by NSE (Fig. 7). The trajectory plot (Fig. 11) shows molecular trapping in the very small section of the sinusoidal channel between intersections
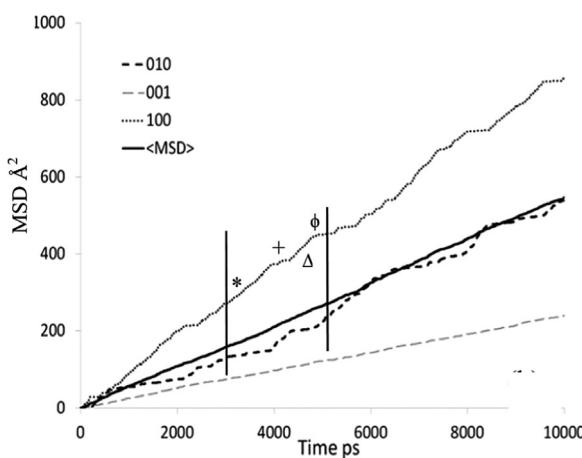

Fig. 10 MSD plot in all directions of an individual isobutane molecule in silicalite-1 at 450 K. Each symbol signifies the assigned portion of the trajectory plot shown in Fig. 11. Reproduced from ref. 59 with permission from the American Chemical Society.
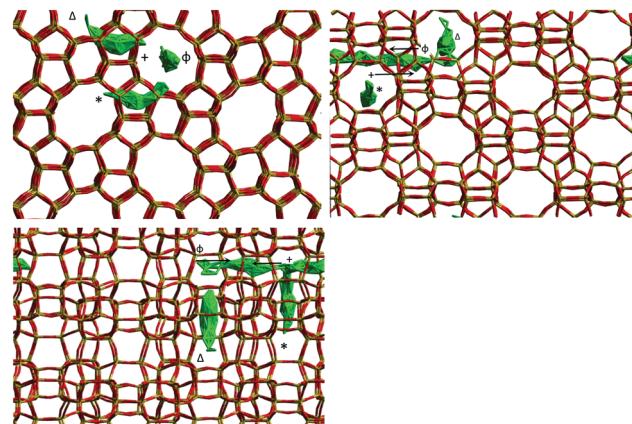
Fig. 11 Trajectory plot of isobutane in silicalite-1 at 450 K between 3000 ps and 5000 ps of the MD simulation run. The symbols represent the appropriate portion of the associated MSD plot in Fig. 10. Reproduced from ref. 59 with permission from the American Chemical Society.

(*ca.* 3 Å in length), then movement between two adjacent sinusoidal channel segments *via* the straight channel segment connecting them.

The movement in the $\langle 100 \rangle$ direction is clearly consistent with the experimentally observed jump diffusion mechanism, but between sinusoidal segments. The 10 Å jump length between sinusoidal segments matches that observed in the NSE experiments. This preference for molecular siting in the sinusoidal channels was attributed to the favourable interactions between the molecule and channel walls, enabled by the increased access and geometric freedom offered by the use of a flexible silicalite-1 framework, absent from previous simulations performed with configurational-bias Monte Carlo and non-equilibrium molecular dynamics[61,62]

The breathing of the framework in this simulation allows for both sustained access, and framework relaxation around the isobutane accommodating this preferred siting. The isobutane then makes the 10 Å jumps between adjacent sections of sinusoidal channel. This study illustrates how the use of more sophisticated MD models can not only give accurate quantitative agreement with QENS/NSE, but may reveal different qualitative behaviours of the sorbate upon comparison with neutron data.

4. QENS and INS studies of the methanol-to-hydrocarbon (MTH) process

The industrial conversion of alcohols to hydrocarbons was first commercialised in the Mobil methanol-to-gasoline process using an HZSM-5 catalyst, in New Zealand in 1986.[63] The availability of cheap methanol derived from natural gas was the initial driver for these technologies. In the future, biomass and other renewable resources are likely to provide a ready supply of methanol, *via* gasification and subsequent hydrogenation of CO/CO$_2$.

The mechanism is generally believed[64] to be *via* a 'hydrocarbon pool' that forms in the pores of the zeolite. At steady-state,
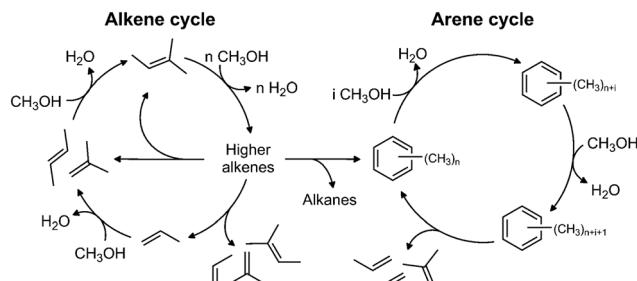
Fig. 12 The dual-cycle mechanism operative in the hydrocarbon pool. Reproduced with permission of Elsevier from: M. Westgård Erichsen, S. Svelle and U. Olsbye, *Catal. Today*, 2013, **215**, 216–223.

Fig. 13 QENS spectra at 298 K of methanol loaded in zeolites H-ZSM-5 and HY at $Q = 0.9$ Å, (--) represents the resolution data taken at 5 K. Reproduced from ref. 65 with permission of the Royal Society of Chemistry.

as shown in Fig. 12, methanol is dehydrated to alkenes, which undergo subsequent reactions to generate methylated aromatics, predominantly methyl benzenes; the dual-cycle' mechanism. Deactivation is by coke formation, which may be graphitic, aromatic or polymeric in nature *i.e.* too large to leave the surface (internal or external) of the zeolite. While a considerable amount of work has been carried out on this important process, there are still many areas of uncertainty including: how does the first C–C bond form; what are the species in the hydrocarbon pool; and what is the nature of the coke? As zeolites are transparent to neutrons, neutron spectroscopy should provide new insight into some of these problems.

The interaction and transport of methanol in H-ZSM-5 is a key issue. QENS is readily able to probe motion in zeolites, so the mobility of methanol in H-ZSM5 and HY was compared[65] HY was chosen because it is inactive for the MTH process and so provides a reference material. We see, Fig. 13, that the two materials behave very differently. The significant broadening in HY is completely consistent with diffusing methanol. MD simulations[29] supported this interpretation and showed the presence of hydrogen-bonded methanol in the pores. In contrast, the close fit to the resolution function in H-ZSM-5 suggests that methanol is immobile on the instrumental time scale.

INS spectroscopy enables the differences in the QENS to be rationalised, Fig. 14. Clean HY shows the characteristic hydroxyl stretch, 3720 cm^{-1}, and bend modes, 1095 cm^{-1}, Fig. 14(a). After loading with methanol, Fig. 14(b), new bands appear at 3020, 1495, 1155 and 720 cm^{-1}. Comparison with solid methanol, Fig. 14(c), shows that these are the unresolved C–H and O–H stretch modes, the methyl deformation, the methyl rock and the C–O–H deformation respectively. The methanol O–H stretch and deformation modes have broadened and shifted on absorption, consistent with the hydrogen-bonding suggested by the QENS and MD results. For H-ZSM5, Fig. 14(d), the framework hydroxyl modes are at similar positions, 3660 and 1095 cm^{-1}, as in HY. However, on absorption of methanol, Fig. 14(e), while the methyl stretch, deformation and rock are at similar positions to those in HY, the methanol O–H stretch and deformation modes have vanished. These observations suggest that complete conversion of methanol to framework methoxy has occurred, which is remarkable, as methanol was introduced at 298 K; thus methoxylation of the Brønsted acid sites, the first step in the
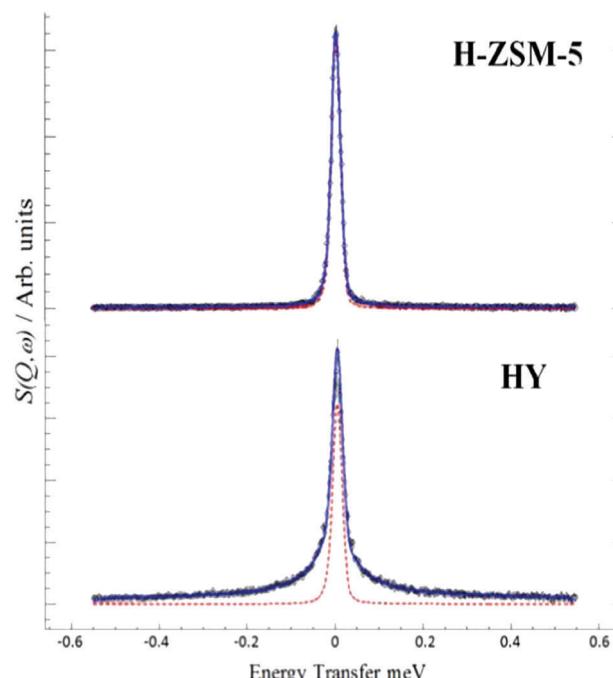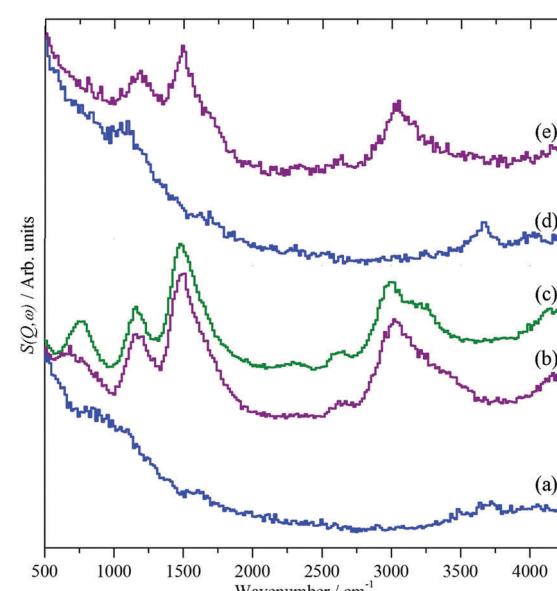

Fig. 14 INS spectra of methanol loaded in zeolites HY and H-ZSM-5.[65] (a) Clean HY, (b) HY + methanol, (c) solid methanol, (d) clean H-ZSM5 and (e) H-ZSM5 + methanol.

MTH process, has occurred at room temperature contrary to studies using more conventional spectroscopy techniques[66–68] and modelling studies[69–72] which suggest a significant energy barrier to the process.

INS spectroscopy has also been used to investigate the working catalyst.[73,74] A series of samples[74] with different time and temperature on-stream were prepared using the react-and-quench method.

These experiments used the reactor[75] that had been developed to carry out reactions on the 10 g scale required for INS rather than the 10 mg scale used in conventional microreactor studies. The samples were characterised by a battery of techniques (infrared spectroscopy, temperature programmed oxidation (to determine carbon content), EPR and GC-MS analysis of the downstream catch-pot used to collect the liquid products (water and hydrocarbons)).

Fig. 15 shows the results of different preparation conditions. Two INS spectrometers were used for the work:[74] green traces are from an instrument with good resolution and modest sensitivity, blue from one with modest resolution and high sensitivity. The catalyst was activated by dehydration at 350 °C in flowing helium, Fig. 15(a). As expected, these results just show the hydroxyls of the Brønsted acid sites. The bending mode shows two components at 1130 and 1185 cm^{-1}, suggesting there may be two distinct sites.

After one hour on-stream at 350 °C, on-line mass spectroscopy[74] shows that the catalyst is producing predominantly olefins. The infrared spectrum[74] indicates that the hydroxyl groups are largely unchanged and shows the presence of a weak peak at 2920 cm^{-1}, assigned to aliphatic species. The INS spectra, Fig. 15(b), shows the hydroxyls and a C–H stretch peak

at 3040 cm^{-1}. The transition energy indicates this hydrocarbonaceous moiety to be olefinic/aromatic in nature, *i.e.* C(sp^2)H. In both infrared and INS spectroscopies, the intensity is directly proportional to the number of oscillators present, however, in the infrared the intensity is weighted by the extinction coefficient, which is a molecular property, so it is different for aliphatic C–H, aromatic C–H and hydroxyl O–H vibrations. In contrast, for INS the weighting is by the amplitude of vibration, which in the harmonic approximation is about the same for both C–H and O–H vibrations, so that the intensities directly reflect the number of oscillators present.

Under our conditions, at 350 °C, the catalyst reaches steady state in a few hours. After 3 days at 350 °C, Fig. 15(c), the O–H stretch mode has largely disappeared and the spectrum is dominated by peaks at 2990 and 3090 cm^{-1}, indicating a co-existence of sp^2 and sp^3 hybridised C–H bonds. The INS relative intensities of the C(sp^3)–H and C(sp^2)–H modes are approximately equal, implying equal numbers of each. It is noted that this is inconsistent with the presence of only polymethylated aromatics, which should have a larger number of aliphatic C–H moieties. In the deformation region there are peaks at 1639, 1460, 1390, and 1190 cm^{-1} and a broad feature at 800–1100 cm^{-1}. The 1460, 1390, and 1190 cm^{-1} modes are assigned as the methyl asymmetric bend, symmetric bend, and rock, respectively of methylated aromatic species.

Fig. 15(d) shows the results after 3 days reaction at 400 °C. The higher temperature was chosen in order to produce a deactivated catalyst, which did not happen and the catalyst was still working when the reaction was stopped. A strong C–H feature is present at 3095 cm^{-1}, with the peak maximum implying a predominance of C(sp^2)H species; the only indication for the presence of C(sp^3)H moieties is that the peak is asymmetric to the low energy side. In the fingerprint region, the spectrum resembles that of the 3 days at 350 °C sample, Fig. 15(c). Three new features at 1090, 939 and 782 cm^{-1} are present, which are thought to arise from aryl C–H wag vibrations and may indicate a contribution from naphthalenic species, which are observed in the catch-pot. This may reflect a change in the balance between the two parts of the dual-cycle mechanism, Fig. 12.

These initial investigations show that INS spectroscopy does indeed offer a way to see unseen features of the MTH process. It enables the fingerprint region to be observed, which is inaccessible to infrared spectroscopy because of the intense framework absorption. In the C–H/O–H stretch region, it allows relative populations to be assessed quantitatively. The samples described here have carbon contents in the range 2–8 wt%, INS will be even more useful for deactivated samples where the coke content reaches 14–18 wt%,[76] and the samples are completely black.

Fig. 15 INS spectra of H-ZSM5 under different conditions for the MTH reaction.[74] (a) The clean catalyst after dehydration at 350 °C and after reaction with methanol at: (b) 350 °C for 1 hour, (c) 350 °C for 3 days and (d) 400 °C for 3 days. Upper part: the C–H and O–H stretch region. Lower part: the fingerprint region.

5. INS studies of methane reforming

With oil reserves diminishing and significant volatility in the price of oil, interest in methane both as a fuel and as a chemical feedstock is growing. To exploit methane in this manner,

its conversion to synthesis gas is a common requirement, which commercially is carried out using steam as the oxidant (steam reforming):

$$CH_4 + H_2O \rightarrow CO + 3H_2 \qquad (9)$$
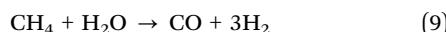
This reaction is endothermic; consequently, it is very energy intensive. An alternative process is to use CO_2 as the oxidant (dry reforming):

$$CH_4 + CO_2 \rightarrow 2CO + 2H_2 \qquad (10)$$
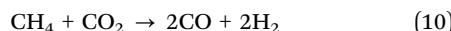
This reaction is also endothermic, but less so than steam reforming when the steam is generated by vaporisation of water. The process also has obvious 'green' credentials, although even if all methane reforming used CO_2, the impact on global CO_2 would be very small.

Nickel catalysts are most commonly used for both steam and dry reforming, but are susceptible to coking which results in catalyst deactivation. The extent of carbon retention by the reforming catalyst can be analysed by temperature programmed oxidation. However, it is much more difficult to determine the amount of retained hydrogen in the carbonaceous overlayer. The presence of large amounts of coke means that infrared spectroscopy is very difficult (but not impossible).[77] Coke does not impede INS spectroscopy and it was expected that the technique would aid characterisation of the coke, which proved correct and INS was used to investigate how variations in reaction conditions, catalyst preparation and oxidant (dry or steam reforming) modified the carbonaceous overlayer.[77–82]

One of the goals was to both speciate and quantify[78] the hydrogen retained by the catalyst. In the harmonic approximation, the amplitude of vibration, U_i, of mode ω_i is given by:

$$(U_i)^2 = \frac{\hbar}{2\mu\omega_i} \qquad (11)$$

where $\hbar$ is Planck's constant, μ is the reduced mass and for a hydrogenous species, $\mu \approx 1$. Thus the intensity per oscillator depends only on the transition energy and is independent of the molecular entity. The result is that a calibration is transferable between species with modes at similar transition energies.

Fig. 16 shows the INS spectrum (2500–4000 cm^{-1}) of a Ni(45%)/Al$_2$O$_3$ catalyst after undergoing 'dry' reforming of methane at 1073 K for six hours.[78] There is a weak C–H stretch peak at 2935 cm^{-1} and a stronger O–H stretch at 3339 cm^{-1}. Quantification of both peaks was possible using polystyrene and Mg(OH)$_2$ as calibrants fpr the C–H and O–H stretch regions, respectively.

Fig. 17 compares the results of dry reforming[80] and steam reforming[82] at 898 K, both using a Ni(26%)/Al$_2$O$_3$ catalyst. In comparison with Fig. 16, the low signal-to-noise ratio indicates that there is considerably less hydrogen present, which is confirmed by the quantitation: the C:H ratios are: 160:1, 2550:1 and 11 690:1 for Fig. 16, 17(a) and (b) respectively. Table 1 shows how different conditions can drastically alter the nature of the hydrocarbonaceous overlayer, both in terms of the amount of retained hydrogen and the type of carbon generated.
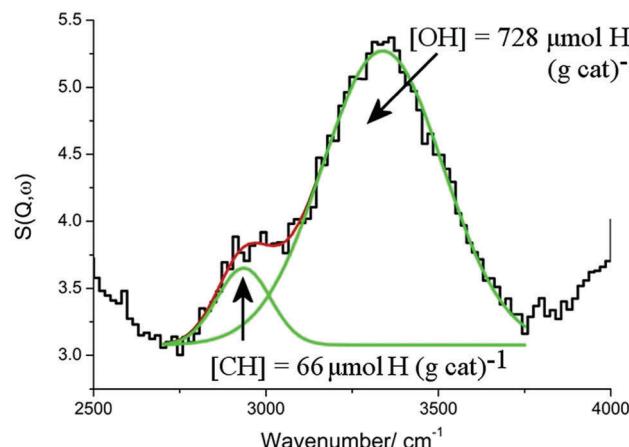
Fig. 16 The INS spectrum (2500–4000 cm^{-1}) of a Ni(45%)/Al$_2$O$_3$ catalyst after undergoing 'dry' reforming of methane at 1073 K for six hours. The experimental data are well described by a combination of two Gaussian curves (green lines) centred at 2935 and 3339 cm^{-1}, which are obtained from a non-linear least squares fitting procedure. The solid red line represents the overall fit. Adapted from ref. 78 by permission of the PCCP Owner Societies.
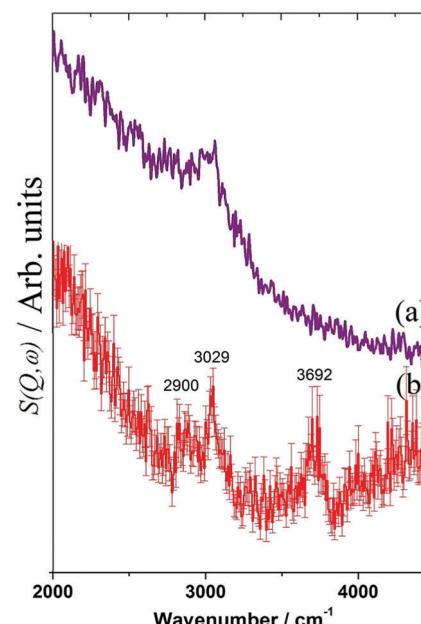
Fig. 17 INS spectra of a Ni(26%)/Al$_2$O$_3$ catalyst after (a) dry reforming and (b) steam reforming of methane at 898 K for six hours.

The picture that emerges is that the catalysts are very efficient at cycling hydrogen but much less so for carbon.

The susceptibility of Ni-based catalysts to coking has led to a search for alternatives. Ru and Rh are more resistant to carbon deposition but are uneconomic for large-scale industrial applications. Co may also be used for dry reforming and it has been reported that Ni–Co bimetallic catalysts offer enhanced performance over the single metal catalysts.

Fig. 18 compares the INS spectra[81] of 25 wt% Ni/Al$_2$O$_3$, Co/Al$_2$O$_3$ and Ni(Co)/Al$_2$O$_3$ (Ni:Co molar ratio 4:1). The different

Table 1 Methane reforming catalysts used

Metal loading/wt%	Source of α-Al$_2$O$_3$ support	Reforming reaction	CH$_4$:CO$_2$	Reaction temperature/K	Type of carbon produced	C:H
45	Sumitomo Chemical	Dry	2:1	1073	Amorphous	160:1
26	Alfa Aesar	Dry	1:1	898	Filamentous	2550:1
26	Alfa Aesar	Steam		898	Filamentous	11 690:1
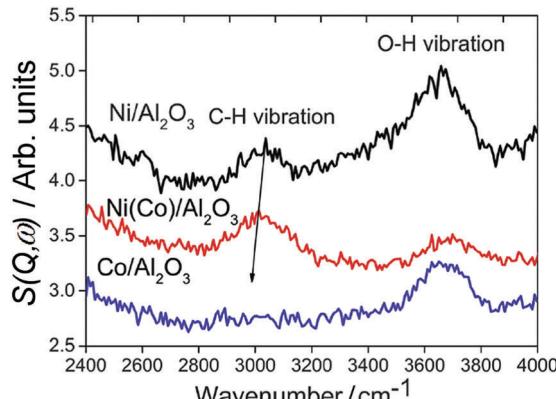
Fig. 18 INS spectra of methane reforming catalysts after dry reforming at 873 K for six hours. Reproduced from ref. 81 by permission of the PCCP Owner Societies.

intensities of the OH stretch modes implies that the catalysts possess different acidity, in the order Ni/Al$_2$O$_3$ > Co/Al$_2$O$_3$ > Ni(Co)/Al$_2$O$_3$. An acidic surface favours catalyst coking in dry reforming and thus it is reasonable to infer that more carbon will be deposited on the Ni/Al$_2$O$_3$ catalyst, compared to the Co/Al$_2$O$_3$ and the bimetallic catalyst. INS features at around 3000 cm^{-1} are assigned to C–H stretch vibrations of unsaturated aromatic moieties. The C–H vibration for the bimetallic Ni–Co catalyst is red-shifted with respect to that for the pure Ni catalyst, suggesting a larger contribution from aliphatic species. The 3000 cm^{-1} vibration is absent from the spent Co/Al$_2$O$_3$ catalyst although a very weak vibration is present at 2900 cm^{-1}, due to aliphatic moieties. The INS spectra reveal that relatively less aromatic carbonaceous but more aliphatic species are deposited on spent Co/Al$_2$O$_3$ and Ni(Co)/Al$_2$O$_3$ catalysts, in comparison to the pure Ni catalyst. The formation of filamentous carbon is more associated with the presence of highly polymerized aromatic species and the preference to aliphatic carbon on Co/Al$_2$O$_3$ catalyst is a significant factor for its resistance to coking.

INS spectroscopy provides a different perspective of adsorbates on catalysts. It is, of course, a complementary technique and it is essential that is backed-up by a range of physical, spectroscopic and electron microscopic methods, as in the work summarised here.

6. Conclusions

This review has, we hope, illustrated the unique power of neutron spectroscopy in probing the translational and vibrational dynamics of key molecular processes in catalytic systems.

The ability of quasielastic techniques to measure molecular transport in catalysts is we consider, of growing importance in view of the increasingly clear significance of such transport processes in controlling catalytic processes. And as we have shown, vibrational spectroscopy with neutrons can interrogate sorbed molecules in environments which would be inaccessible to other spectroscopies and can provide data for modes and energies that cannot be reached by photon based techniques. Neutron spectroscopy will play a vital role in developing a detailed understanding of the molecular level processes in real catalytic reactions.

The reader may find more recent examples of the applications of neutrons in catalysis in the recently published special issue of *Physical Chemistry, Chemical Physics* which is devoted to this topic.[83]

Conflicts of interest

There are no conflicts to declare.

Acknowledgements

References

1 P. A. Wright, J. M. Thomas, A. K. Cheetham and A. K. Nowak, *Nature*, 1985, **318**, 611–614.
2 R. Goyal, A. Fitch and H. Jobic, *J. Phys. Chem. B*, 2000, **104**, 2878–2884.
3 M. Falkowska, S. Chansai, H. G. Manyar, L. F. Gladden, D. T. Bowron, T. G. Youngs and C. Hardacre, *Phys. Chem. Chem. Phys.*, 2016, **18**, 17237–17243.
4 M. E. Potter, A. J. O'Malley, S. Chapman, J. Kezina, S. H. Newland, I. P. Silverwood, S. Mukhopadhyay, M. Carravetta, T. M. Mezza, S. F. Parker, C. R. A. Catlow and R. Raja, *ACS Catalysis*, 2017, **7**, 2926–2934.
5 M. E. Potter, S. Chapman, A. J. O'Malley, A. Levy, M. Carravetta, T. M. Mezza, S. F. Parker and R. Raja, *ChemCatChem*, 2017, **9**, 1897–1900.

This journal is © The Royal Society of Chemistry 2017

6 J. Niemantsverdriet, *Spectroscopy in Catalysis: An Introduction*, 3rd edn, Wiley-VCH Verlag GmbH & Co. KGaA, 2007, pp. 179–216.
7 P. C. H. Mitchell, S. F. Parker, A. J. Ramirez-Cuesta and J. Tomkinson, *Vibrational spectroscopy with neutrons: with applications in chemistry, biology, materials science and catalysis*, World Scientific, 2005.
8 C. G. Windsor, *J. Appl. Crystallogr.*, 1988, **21**, 582–588.
9 T. G. Youngs, H. Manyar, D. T. Bowron, L. F. Gladden and C. Hardacre, *Chem. Sci.*, 2013, **4**, 3484–3489.
10 J. Daillant and A. Gibaud, *X-ray and neutron reflectivity: principles and applications*, Springer, 2008.
11 B. T. M. Willis and C. J. Carlile, *Experimental neutron scattering*, Oxford University Press, 2017.
12 P. W. Albers, D. Lennon and S. F. Parker, in *Neutron Scattering - Applications in Biology, Chemistry, and Materials Science*, ed. F. Fernando-Alonso and D. L. Price, Experimental Methods in the Physical Sciences, Academic Press, 2017, ch. 5, vol. 49, pp. 279–348.
13 S. F. Parker, *Chem. Commun.*, 2011, **47**, 1988–1990.
14 R. Juárez, S. F. Parker, P. Concepción, A. Corma and H. García, *Chem. Sci.*, 2010, **1**, 731–738.
15 H. Jobic and D. N. Theodorou, *Microporous Mesoporous Mater.*, 2007, **102**, 21–50.
16 M. Bée, *Quasielastic Neutron Scattering*, Adam Hilger, 1988.
17 A. J. O'Malley and C. R. A. Catlow, in *Neutron Scattering - Applications in Biology, Chemistry, and Materials Science*, ed. F. Fernando-Alonso and D. L. Price, Experimental Methods in the Physical Sciences, Academic Press, 2017, ch. 6, vol. 49, pp. 349–401.
18 C. Chudley and R. Elliott, *Proc. Phys. Soc., London*, 1961, **77**, 353.
19 K. Singwi and A. Sjölander, *Phys. Rev.*, 1960, **119**, 863.
20 N. K. Kanellopoulos, *Recent advances in gas separation by microporous ceramic membranes*, Elsevier, 2000.
21 F. Mezei, in *Neutron Spin Echo*, ed. F. Mezei, Lecture Notes in Physics, Springer-Verlag, Berlin, 1980, vol. 122.
22 H. Jobic, A. Méthivier and G. Ehlers, *Microporous Mesoporous Mater.*, 2002, **56**, 27–32.
23 H. Jobic, M. Bée and S. Pouget, *J. Phys. Chem. B*, 2000, **104**, 7130–7133.
24 P. D. Kolokathis, G. R. Káli, H. Jobic and D. N. Theodorou, *J. Phys. Chem. C*, 2016, **120**, 21410–21426.
25 A. J. O'Malley, I. Hitchcock, M. Sarwar, I. P. Silverwood, S. Hindocha, C. R. A. Catlow, A. P. York and P. Collier, *Phys. Chem. Chem. Phys.*, 2016, **18**, 17159–17168.
26 R. Mukhopadhyay, A. Sayeed, S. Mitra, A. A. Kumar, M. N. Rao, S. Yashonath and S. Chaplot, *Phys. Rev. E: Stat., Nonlinear, Soft Matter Phys.*, 2002, **66**, 061201.
27 A. Sayeed, S. Mitra, A. Anil Kumar, R. Mukhopadhyay, S. Yashonath and S. Chaplot, *J. Phys. Chem. B*, 2003, **107**, 527–533.
28 L. N. Gergidis, D. N. Theodorou and H. Jobic, *J. Phys. Chem. B*, 2000, **104**, 5541–5552.
29 A. J. O'Malley, V. G. Sakai, I. P. Silverwood, N. Dimitratos, S. F. Parker and C. R. A. Catlow, *Phys. Chem. Chem. Phys.*, 2016, **18**, 17294–17302.
30 S. M. Auerbach, K. A. Carrado and P. K. Dutta, *Handbook of zeolite science and technology*, CRC Press, 2003.
31 E. Vogt and B. Weckhuysen, *Chem. Soc. Rev.*, 2015, **44**, 7342–7370.
32 J. Weitkamp and L. Puppe, *Catalysis and zeolites: fundamentals and applications*, Springer Science & Business Media, 2013.
33 B. Smit and T. L. Maesen, *Chem. Rev.*, 2008, **108**, 4125–4184.
34 M. Jiang, M. Eic, S. Miachon, J.-A. Dalmon and M. Kocirik, *Sep. Purif. Technol.*, 2001, **25**, 287–295.
35 F. Leroy, B. Rousseau and A. Fuchs, *Phys. Chem. Chem. Phys.*, 2004, **6**, 775–783.
36 R. Krishna and J. Van Baten, *Chem. Eng. J.*, 2008, **140**, 614–620.
37 A. O. Koriabkina, A. M. de Jong, D. Schuring, J. van Grondelle and R. A. van Santen, *J. Phys. Chem. B*, 2002, **106**, 9559–9566.
38 M. Yu, J. C. Wyss, R. D. Noble and J. L. Falconer, *Microporous Mesoporous Mater.*, 2008, **111**, 24–31.
39 J. Fried and S. Weaver, *Comput. Mater. Sci.*, 1998, **11**, 277–293.
40 F. Jianfen, B. Van de Graaf, H. Xiao and S. Njo, *J. Mol. Struct.: THEOCHEM*, 1999, **492**, 133–142.
41 L. Song, Z.-L. Sun and L. V. Rees, *Microporous Mesoporous Mater.*, 2002, **55**, 31–49.

42 A. R. Teixeira, C.-C. Chang, T. Coogan, R. Kendall, W. Fan and P. J. Dauenhauer, *J. Phys. Chem. C*, 2013, **117**, 25545–25555.
43 D. M. Ruthven, M. Eic and E. Richard, *Zeolites*, 1991, **11**, 647–653.
44 R. Q. Snurr and J. Kärger, *J. Phys. Chem. B*, 1997, **101**, 6469–6473.
45 N. Van-Den-Begin, L. V. Rees, J. Caro, M. Bülow, M. Hunger and J. Kärger, *J. Chem. Soc., Faraday Trans. 1*, 1989, **85**, 1501–1509.
46 H. Jobic, *J. Mol. Catal. A: Chem.*, 2000, **158**, 135–142.
47 H. Jobic and D. N. Theodorou, *J. Phys. Chem. B*, 2006, **110**, 1964–1967.
48 F. Leroy and H. Jobic, *Chem. Phys. Lett.*, 2005, **406**, 375–380.
49 H. Jobic, W. Schmidt, C. B. Krause and J. Kärger, *Microporous Mesoporous Mater.*, 2006, **90**, 299–306.
50 E. J. Maginn, A. T. Bell and D. N. Theodorou, *J. Phys. Chem.*, 1996, **100**, 7155–7173.
51 A. J. O'Malley and C. R. A. Catlow, *Phys. Chem. Chem. Phys.*, 2015, **17**, 1943–1948.
52 R. C. Runnebaum and E. J. Maginn, *J. Phys. Chem. B*, 1997, **101**, 6394–6408.
53 A. J. O'Malley and C. R. A. Catlow, *Phys. Chem. Chem. Phys.*, 2013, **15**, 19024–19030.
54 H. Jobic and B. Farago, *J. Chem. Phys.*, 2008, **129**, 171102.
55 B. Millot, A. Méthivier, H. Jobic, H. Moueddeb and M. Bée, *J. Phys. Chem. B*, 1999, **103**, 1096–1101.
56 H. Jobic, M. Bée and J. Caro, in *Proceedings of the 9th International Zeolite Conference, Montreal, 1992*, ed. R. von Ballmoos, J. B. Higgins and M. M. Treacy, Butterworth-Heinemann, Boston, 1993, vol. II, p. 121.
57 H. Jobic, M. Bée and G. J. Kearley, *Zeolites*, 1989, **9**, 312–317.
58 H. Jobic, M. Bée and G. J. Kearley, *Zeolites*, 1992, **12**, 146–151.
59 A. J. O'Malley, C. R. A. Catlow, M. Monkenbusch and H. Jobic, *J. Phys. Chem. C*, 2015, **119**, 26999–27006.
60 H. Jobic, M. Bée and S. Pouget, *J. Phys. Chem. B*, 2000, **104**, 7130–7133.
61 T. Vlugt, W. Zhu, F. Kapteijn, J. Moulijn, B. Smit and R. Krishna, *J. Am. Chem. Soc.*, 1998, **120**, 5599–5600.
62 S. Furukawa, C. McCabe, T. Nitta and P. Cummings, *Fluid Phase Equilib.*, 2002, **194**, 309–317.
63 C. Maiden, *Stud. Surf. Sci. Catal.*, 1988, **36**, 1–16.
64 U. Olsbye, S. Svelle, K. Lillerud, Z. Wei, Y. Chen, J. Li, J. Wang and W. Fan, *Chem. Soc. Rev.*, 2015, **44**, 7155–7176.
65 A. J. O'Malley, S. F. Parker, A. Chutia, M. R. Farrow, I. P. Silverwood, V. García-Sakai and C. R. A. Catlow, *Chem. Commun.*, 2016, **52**, 2897–2900.
66 T. R. Forester, S.-T. Wong and R. F. Howe, *J. Chem. Soc., Chem. Commun.*, 1986, 1611–1613.
67 T. Forester and R. F. Howe, *J. Am. Chem. Soc.*, 1987, **109**, 5076–5082.
68 L. Kubelková, J. Nováková and K. Nedomová, *J. Catal.*, 1990, **124**, 441–450.
69 J. Van der Mynsbrugge, S. L. Moors, K. De Wispelaere and V. Van Speybroeck, *ChemCatChem*, 2014, **6**, 1906–1918.
70 J. Andzelm, N. Govind, G. Fitzgerald and A. Maiti, *Int. J. Quantum Chem.*, 2003, **91**, 467–473.
71 C. Zicovich-Wilson, P. Viruela and A. Corma, *J. Phys. Chem.*, 1995, **99**, 13224–13231.
72 A. J. O'Malley, A. Logsdail, A. Sokol and C. R. A. Catlow, *Faraday Discuss.*, 2016, **188**, 235–255.
73 R. F. Howe, J. McGregor, S. F. Parker, P. Collier and D. Lennon, *Catal. Lett.*, 2016, **146**, 1242–1248.
74 Suwardiyanto, R. F. Howe, E. K. Gibson, C. R. A. Catlow, A. Hameed, J. McGregor, P. Collier, S. F. Parker and D. Lennon, *Faraday Discuss.*, 2017, **197**, 447–471.
75 R. Warringham, D. Bellaire, S. Parker, J. Taylor, R. Ewings, C. Goodway, M. Kibble, S. Wakefield, M. Jura and M. Dudman, *J. Phys.: Conf. Ser.*, 2014, **54**, 012005.
76 D. Bibby, N. Milestone, J. Patterson and L. Aldridge, *J. Catal.*, 1986, **97**, 493–502.
77 I. P. Silverwood, N. G. Hamilton, J. Z. Staniforth, C. J. Laycock, S. F. Parker, R. M. Ormerod and D. Lennon, *Catal. Today*, 2010, **155**, 319–325.
78 I. P. Silverwood, N. G. Hamilton, C. J. Laycock, J. Z. Staniforth, R. M. Ormerod, C. D. Frost, S. F. Parker and D. Lennon, *Phys. Chem. Chem. Phys.*, 2010, **12**, 3102–3107.

79 I. P. Silverwood, N. G. Hamilton, A. R. McFarlane, J. Kapitán, L. Hecht, E. L. Norris., R. M. Ormerod, C. D. Frost, S. F. Parker and D. Lennon, *Phys. Chem. Chem. Phys.*, 2012, **14**, 15214–15225.

80 A. R. McFarlane, I. P. Silverwood, R. Warringham, E. L. Norris, R. M. Ormerod, C. D. Frost, S. F. Parker and D. Lennon, *RSC Adv.*, 2013, **3**, 16577–16589.

81 X. Liao, R. Gerdts, S. F. Parker, L. Chi, Y. Zhao, M. Hill, J. Guo, M. O. Jones and Z. Jiang, *Phys. Chem. Chem. Phys.*, 2016, **18**, 17311–17319.

82 A. R. McFarlane, I. P. Silverwood, E. L. Norris, R. M. Ormerod, C. D. Frost, S. F. Parker and D. Lennon, *Chem. Phys.*, 2013, **427**, 54–60.

83 I. P. Silverwood, S. F. Parker and C. R. A. Catlow, *Phys. Chem. Chem. Phys.*, 2016, **18**.